

## Phase and contrast moiré signatures in two-dimensional cone beam interferometry

D. Sarenac<sup>1,2,\*</sup>, G. Gorbet<sup>3</sup>, Charles W. Clark<sup>4</sup>, D. G. Cory<sup>2,5</sup>, H. Ekinici<sup>6</sup>, M. E. Henderson<sup>2,3</sup>, M. G. Huber<sup>6</sup>,  
D. S. Hussey<sup>6</sup>, C. Kapahi<sup>2,3</sup>, P. A. Kienzle<sup>6</sup>, Y. Kim<sup>6,7</sup>, A. M. Long<sup>8</sup>, J. D. Parker<sup>9</sup>, T. Shinohara<sup>10</sup>,  
F. Song<sup>10</sup> and D. A. Pushin<sup>2,3,†</sup>

<sup>1</sup>Department of Physics, University at Buffalo, State University of New York, Buffalo, New York 14260, USA

<sup>2</sup>Institute for Quantum Computing, University of Waterloo, Waterloo, Ontario, Canada N2L3G1

<sup>3</sup>Department of Physics, University of Waterloo, Waterloo, Ontario, Canada N2L3G1

<sup>4</sup>Joint Quantum Institute, National Institute of Standards and Technology and University of Maryland, College Park, Maryland 20742, USA

<sup>5</sup>Department of Chemistry, University of Waterloo, Waterloo, Ontario, Canada N2L3G1

<sup>6</sup>National Institute of Standards and Technology, Gaithersburg, Maryland 20899, USA

<sup>7</sup>University of Maryland, College Park, Maryland 20742, USA

<sup>8</sup>Materials Science and Technology Division, Los Alamos National Laboratory, Los Alamos, New Mexico 87545, USA

<sup>9</sup>Neutron Science and Technology Center, Comprehensive Research Organization for Science and Society (CROSS), 162-1 Shirakata, Tokai, Ibaraki 319-1106, Japan

<sup>10</sup>J-PARC Center, Japan Atomic Energy Agency (JAEA), 2-4 Shirakata, Tokai, Ibaraki 319-1195, Japan



(Received 1 February 2024; revised 4 June 2024; accepted 7 August 2024; published 5 September 2024)

Neutron interferometry has played a distinctive role in fundamental science and characterization of materials. Moiré neutron interferometers are candidate next-generation instruments: they offer microscopy-like magnification of the signal, enabling direct camera recording of interference patterns across the full neutron wavelength spectrum. Here we demonstrate the extension of phase-grating moiré interferometry to two-dimensional geometries. Our fork-dislocation phase gratings reveal phase singularities in the moiré pattern, and we explore orthogonal moiré patterns with two-dimensional phase gratings. Our measurements of phase topologies and gravitationally induced phase shifts are in good agreement with theory. These techniques can be implemented in existing neutron instruments to advance interferometric analyses of emerging materials and precision measurements of fundamental constants.

DOI: [10.1103/PhysRevResearch.6.L032054](https://doi.org/10.1103/PhysRevResearch.6.L032054)

**Introduction.** Perfect-crystal neutron interferometry possesses a prestigious record of high impact fundamental science experiments such as the observation of gravitationally induced quantum interference [1],  $4\pi$  symmetry of spinor rotation [2], neutron triply entangled GHZ states and quantum discord [3,4], matter-wave orbital angular momentum [5,6], and the probing of dark energy and fifth forces [7,8]. This is in part because of the unique properties of the neutron such as its electrical neutrality, relatively large mass, angstrom sized wavelengths, extremely low polarizability, and the practical absence of Casimir and van der Waals forces [9–12]. Such properties also make the neutron a convenient and indispensable probe of modern materials as they are capable of characterizing bulk properties and nanometer-sized spin textures [13–16].

A recent focus in neutron interferometry has been in grating-based setups that are capable of working in the full spectrum of the neutron beam [17–23], and circumvent the stringent environmental isolating requirements associated with perfect-crystal neutron interferometry such as mK temperature stability and translational stability on the order of the crystal lattice constant [24,25]. The backbone of these setups is the near-field phenomena of self-imaging known as the “Talbot effect” [26]. Further developments introduced phase-grating moiré interferometers (PGMIs) that are composed of exclusively phase gratings and manifest interference patterns that are directly detectable via typical neutron camera [27–32].

Here we introduce and quantify two-dimensional (2D) moiré interference. We explore the role of phase singularities that materials possessing helical structures are expected to induce in the moiré pattern and we describe the additional metrics for quantification. Furthermore, we also demonstrate 2D moiré interference with orthogonal directionality. The addition of an interference pattern serving as *in situ* reference enables novel approaches for high-precision measurements of fundamental forces such as the Newtonian constant of gravitation.

**Results and discussion.** We fabricated four types of phase gratings: 2D phase gratings, and fork-dislocation

\*Contact author: [dusansar@buffalo.edu](mailto:dusansar@buffalo.edu)

†Contact author: [dmitry.pushin@uwaterloo.ca](mailto:dmitry.pushin@uwaterloo.ca)

Published by the American Physical Society under the terms of the Creative Commons Attribution 4.0 International license. Further distribution of this work must maintain attribution to the author(s) and the published article's title, journal citation, and DOI.

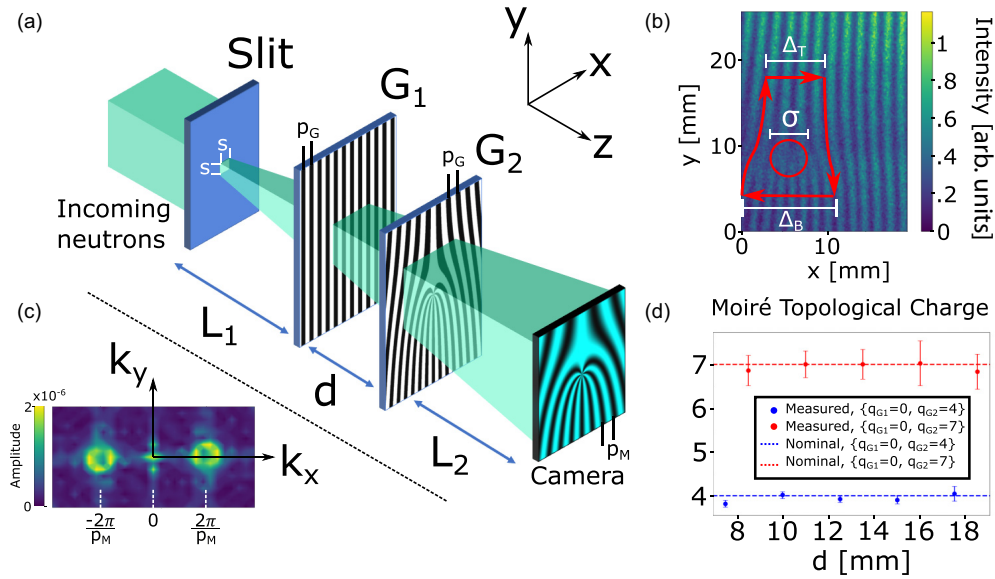


FIG. 1. (a) The two-PGMI setup with fork-dislocation phase gratings. In our experiments we employed and characterized  $\{q_{G_1}=0, q_{G_2}=4\}$  and  $\{q_{G_1}=0, q_{G_2}=7\}$  configurations. The moiré pattern at the camera manifests a phase singularity with a topological charge of  $q_M = \Delta q_G$  and with moiré period of  $p_M = Lp_G/d$ , where  $L$  is the distance from the slit to camera,  $p_G$  is the period of the phase gratings, and  $d$  is the distance between the two phase gratings. For the given parameters,  $p_M$  that results in the highest contrast spans a range of to 1.3 mm to 3.6 mm. (b) An example of the measured intensity profile where the size of the blur ( $\sigma$ ) centered on the phase singularity is determined by the size of the slit ( $s$ ). A convenient method of determining the topology in the measured intensity profile is given by  $q_M = N_B - N_T$  where  $N_B(N_T)$  is the number of periods in a segment  $\Delta_B(\Delta_T)$  below (above) the origin where the connecting vertical lines (red arrows) between the two segments follow a trajectory of constant intensity [33]. (c) The Fourier transform of the intensity pattern shown in (b) possesses doughnut-shaped diffraction orders indicative of helical phase structures [34]. (d) The fitted topological charge of the observed moiré interference in our experiments for the  $\{q_{G_1}=0, q_{G_2}=4\}$  and  $\{q_{G_1}=0, q_{G_2}=7\}$  configurations. The uncertainties shown are purely from counting statistics.

phase gratings with topological charge of  $q = 0, 4, 7$ . Note that the  $q = 0$  is a typical 1D phase grating. The detailed nanofabrication procedure and scanning electron microscopy (SEM) images of all four cases can be found in the Appendix.

The observed interference pattern at the camera is typically fit to a sinusoid,

$$I = A + B \cos(2\pi x/p_s + \phi_0), \quad (1)$$

where  $p_s$  is the period of the oscillation,  $\phi_0$  is the phase shift, and  $A$  and  $B$  are the mean and the amplitude of the oscillations. The contrast or fringe visibility of the particular frequency  $k_s = 2\pi/p_s$  is given by  $V(k_s) = B/A$ . Furthermore, the contrast could also be computed from the Fourier transform of the intensity profile  $H(k_x)$  where  $V(k_s) = 2|H(k_s)/H(0)|$ .

*Fork-dislocation phase gratings.* Here we explore the effect of helical structures that manifest phase singularities in the moiré pattern by introducing a topological charge onto the phase gratings themselves. A fork-dislocation phase grating with period  $p_G$ , height  $D$ , and topological charge  $q_G$  has the profile

$$\Phi = \frac{Nb_c \lambda D}{2} \text{sgn}[\cos(k_G x + q_G \phi)] \quad (2)$$

where  $k_G = 2\pi/p_G$  is the grating wave vector,  $x(\phi)$  is the Cartesian (azimuthal) coordinate,  $Nb_c$  is the scattering length density of the grating material, and  $\lambda$  is the neutron wavelength. Using the recently introduced  $k$ -space model [35] we can simulate the intensity and contrast behavior using the phase-grating profile of Eq. (2).

An experimental demonstration was performed with the two-PGMI configurations of  $\{q_{G_1}=0, q_{G_2}=4\}$  and  $\{q_{G_1}=0, q_{G_2}=7\}$ . The first configuration is depicted on Fig. 1(a). The moiré pattern at the camera possesses a topological charge of  $q_M = \Delta q_G$  with moiré period of  $p_M = Lp_G/d$ , where  $L$  is the distance from the slit to camera,  $p_G$  is the period of the phase gratings, and  $d$  is the distance between the two phase gratings. The Fourier transform of the intensity profile of Fig. 1(b) is shown in Fig. 1(c) where the doughnut profiles are indicative of helical structures with phase singularities [34].

Whereas contrast is the figure of merit for a 1D two-PGMI, an additional metric is needed for identifying and characterizing phase singularities. In this particular setup the topology in the moiré pattern can be determined by  $q_M = N_B - N_T$  where  $N_B(N_T)$  is the number of periods in a segment  $\Delta_B(\Delta_T)$  below (above) the origin where the connecting vertical lines between the two segments follow a trajectory of constant intensity [33], see Fig. 1(b). Using this method we can calculate the measured moiré topology using a fit procedure for the two experimental configurations as shown in Fig. 1(d). This method becomes increasingly useful as the blur centered on the phase singularity increases with slit size.

Examples of the measured moiré pattern at the camera are shown in the first column of Fig. 2 for both  $\{q_{G_1}=0, q_{G_2}=4\}$  and  $\{q_{G_1}=0, q_{G_2}=7\}$ . The simulated (measured) contrast as a function of phase-grating separation and wavelength is shown in the second (third) column of Fig. 2. The experimentally accessible parameters were not centered around

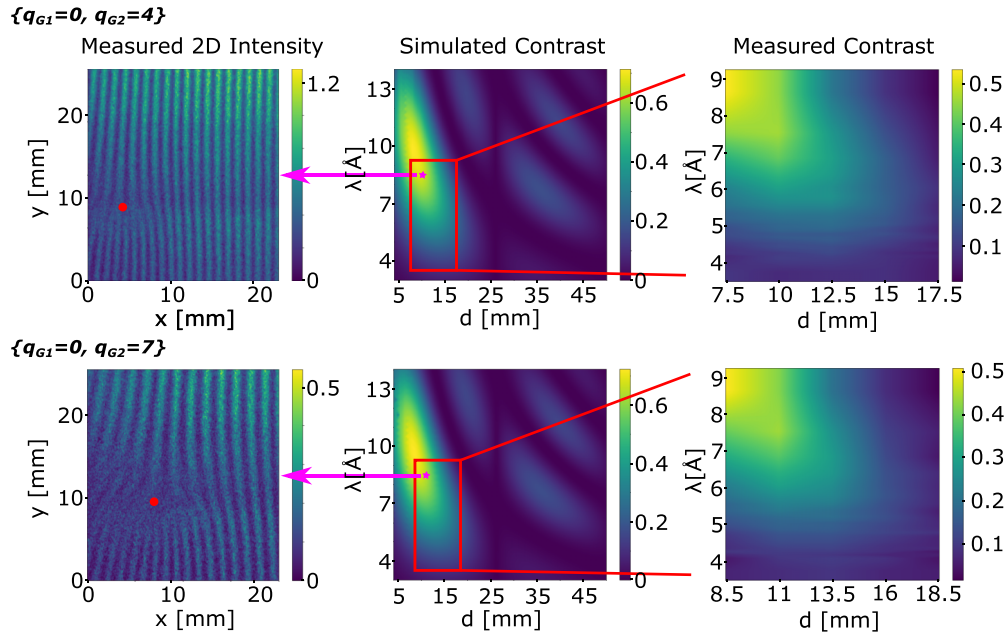


FIG. 2. The intensity and contrast behavior of the two-PGMI setup with fork-dislocation phase gratings. (First column) The observed 2D moiré intensity profile at the camera with the center of the fork-dislocation indicated by the red circle. (Second column) The simulated contrast as a function of wavelength and phase-grating separation distance. Note that the vertical line of zero contrast around  $d = 25$  mm occurs for the configuration where the moiré period at the camera is equal to the slit size. (Third column) The measured contrast for the accessible setup parameters. Top (bottom) row shows the setup for the  $\{q_{G_1} = 0, q_{G_2} = 4\}$  ( $\{q_{G_1} = 0, q_{G_2} = 7\}$ ) configuration. The 2D moiré pattern at the camera manifests a phase singularity with topology  $q_M = \Delta q_G$  as described in Fig. 1. The middle column depicts the contrast behavior for a larger parameter range, and indicates the parameters for the other two columns. The wavelength range for the 2D moiré intensity profiles shown in the first column is  $\lambda = 8 \text{ \AA} - 9 \text{ \AA}$  and the phase-grating separation is  $d = 10 \text{ mm}$  ( $11 \text{ mm}$ ) for the  $\{q_{G_1} = 0, q_{G_2} = 4\}$  ( $\{q_{G_1} = 0, q_{G_2} = 7\}$ ) configuration.

the optimal contrast parameters as the phase gratings were initially designed for a monochromatic  $\lambda = 9 \text{ \AA}$  neutrons. Good agreement is found between the predicted and measured contrast. See the Appendix for supporting data including a plot of the residuals.

**2D phase gratings.** Precision measurements of gravity are a long-standing challenge in metrology, evidenced by the large relative uncertainty in the CODATA value for the gravitational constant ( $G$ ),  $2.2 \times 10^{-5}$ , compared to the Rydberg constant at  $1.9 \times 10^{-12}$ , and the vacuum electric permittivity at  $1.5 \times 10^{-10}$  [36]. While the majority of experiments contributing to the 2018 adjusted CODATA values for  $G$  have achieved a relative precision on the order of  $10^{-5}$ , the relative disagreement between these values is on the order of  $10^{-3}$  [37]. Historically, the measured values contributing to the recommended value of  $G$  have been subject to significant revisions as systematic effects in these experiments are better understood [38,39]. As 12 of the 16 measured values contributing to the 2018 CODATA revised value for  $G$  use some variation of a torsion balance experiment, new methods of measuring  $G$  with independent systematic effects are critical to resolving the aforementioned discrepancies.

Here we aim to explore the 2D moiré pattern that possesses a periodicity along two orthogonal directions, which can make use of the convenient properties of the neutron to perform a high precision measurement of  $G$ . There are many variations possible for 2D phase-grating profiles. For our experiments

we chose a profile of

$$\Phi = \frac{Nb_c\lambda D}{2} \text{sgn}[\cos(k_G x) + \cos(k_G y) - 1], \quad (3)$$

which is essentially a 2D array of circular holes as shown in the SEM images in the Appendix. The setup schematic is depicted on Fig. 3(a). The 2D moiré pattern at the camera possesses a sinusoidal pattern in both the  $x$  and  $y$  directions. Therefore, its Fourier transform shows 2D diffraction orders as depicted in Fig. 3(b). The 2D moiré pattern can be integrated along either Cartesian direction as shown in Fig. 3(c) where we consider the  $y$  axis to be along Earth's gravity and the  $x$  axis along the perpendicular direction. The data shown in Fig. 3(c) is obtained by considering the phase-grating separation of  $d = 12.5 \text{ mm}$  and  $\lambda = 5 \text{ \AA} - 6 \text{ \AA}$  wavelength distribution, and the observed intensity profile at the camera has been rotated by  $\theta = 13.3^\circ$  (corresponding to the maximum contrast location in a contrast vs  $\theta$  plot).

The measured contrast as a function of phase-grating separation ( $d$ ) for a polychromatic wavelength distribution is shown on Figs. 4(a), and 4(b) shows wavelength-dependent contrast for a particular  $d$ . See Appendix for the wavelength distribution profile. Using the k-space model of Ref. [35], it can be confirmed that even when accounting for gravity, the difference between the contrasts along the two directions should have been negligible for the given experimental parameters. The observed difference is most likely attributed to

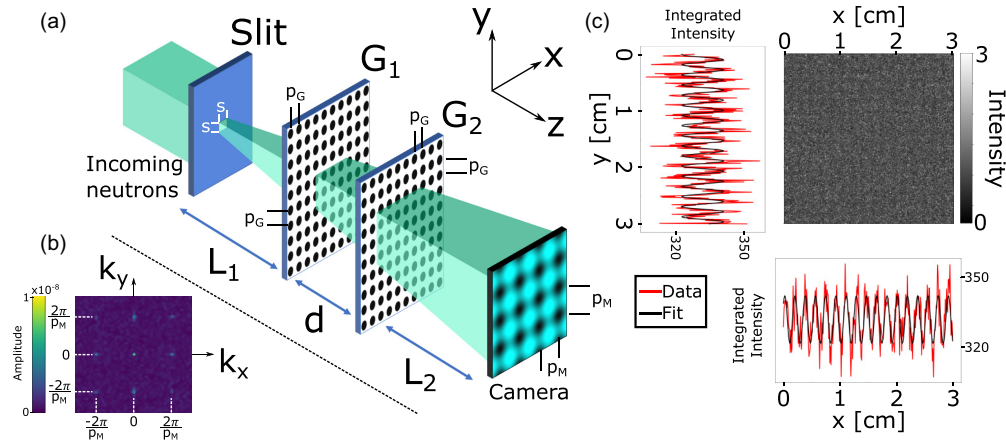


FIG. 3. (a) The two-PGMI setup with two 2D phase gratings. The moiré pattern at the camera manifests a 2D moiré pattern that possesses an  $x$  and  $y$  periodicity of  $p_M = Lp_G/d$ , where  $L$  is the distance from the slit to camera,  $p_G$  is the period of the phase gratings, and  $d$  is the distance between the two phase gratings. For the given parameters,  $p_M$  that results in the highest contrast spans a range of to 1.3 mm to 3.6 mm. (b) The Fourier transform of the intensity pattern shows 2D diffraction orders. (c) The observed intensity profile at the camera can be integrated along  $x$  or  $y$  to independently analyze the contrast along the two orthogonal directions, thereby providing an *in situ* reference signal when considering 1D forces and structures. For example, the value of the gravitational constant ( $G$ ) can, in principle, be extracted from the phase shift induced by placing a well-characterized test mass alongside the interferometer.

the difference in slit sizes. The 2D slit was composed of a sequence of two perpendicular 1D slits each made by bringing two cadmium pieces together with the target gap of  $500\ \mu\text{m}$ . Performing a least squares fit to the two slit sizes we find good agreement with  $642\ \mu\text{m} \pm 7\ \mu\text{m}$  for the slit along  $x$  and  $783\ \mu\text{m} \pm 11\ \mu\text{m}$  for slit along  $y$ . These values are well within the expected experimental uncertainties.

Figure 4(c) shows the wavelength-dependent phase shift that can be used to quantify the effect of gravity. In a two-PGMI the main contribution to the gravitationally induced phase shifts is the neutron fall ( $\Delta_y$ ) between the second phase grating and the neutron camera,

$$\phi_g = \frac{2\pi \Delta_y}{p_M} \cos \theta + C_0 = \frac{\pi g}{p_M} \left( \frac{L_2 m \lambda}{h} \right)^2 \cos \theta + C_0 \quad (4)$$

where  $\theta$  is the angle between the vertical moiré vector and the gravitational force vector,  $g$  is the acceleration caused by Earth’s gravity,  $m$  is the mass of the neutron,  $h$  is the Plank’s constant, and  $C_0$  is an arbitrary offset.

Using the  $k$ -space model described in Ref. [35] we can simulate the expected contrast given the experimental parameters and the addition of the gravitational phase shift term of Eq. (4). In order to analyze the wavelength dependent contributions, we consider the integrated intensity data for each wavelength bin (see Appendix for the wavelength bin parameters). For the fit of the acceleration caused by Earth’s gravity, we obtain  $g = 9.6\ \text{m/s}^2 \pm 0.4\ \text{m/s}^2$ . The low precision of the measurement, which can be drastically improved, was a result of the fact that the gratings were fabricated for a different wavelength spectrum.

With a neutron 2D PGMI, the value of the gravitational constant ( $G$ ) can, in principle, be extracted from the phase

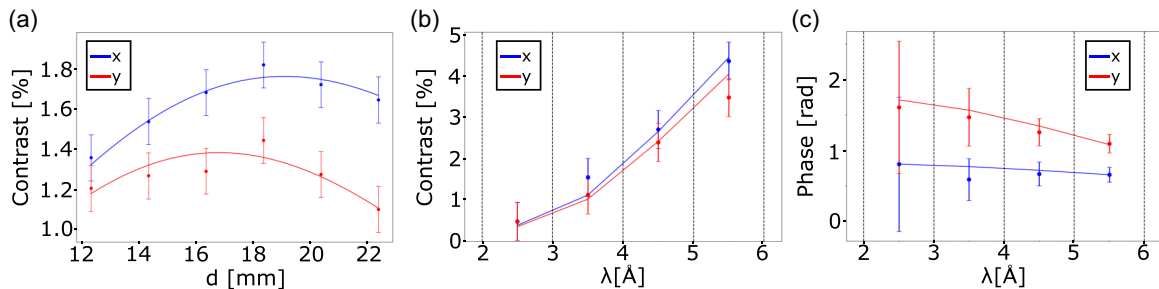


FIG. 4. (a) The measured contrast of the two-PGMI setup with two 2D phase gratings as a function of grating separation distance  $d$  and considering the full polychromatic wavelength distribution (see Appendix). The simulation curves are obtained with the  $k$ -space model [35] for the given experimental parameters and with a least squares fit for the two slit sizes. The best fit is determined for  $642\ \mu\text{m} \pm 7\ \mu\text{m}$  for the slit along  $x$  and  $783\ \mu\text{m} \pm 11\ \mu\text{m}$  for the slit along  $y$ , which is well within the expected experimental error. (b) The wavelength-dependent contrast along the  $x$  and  $y$  direction for  $d = 12.5\ \text{mm}$ . (c) The wavelength-dependent phase shift along the  $x$  and  $y$  direction for  $d = 12.5\ \text{mm}$ . The wavelength distribution around each wavelength interval is shown in the Appendix. We find good agreement with the expected values when taking into account the gravitational fall from the second phase grating to the camera and the relative rotation of  $\theta = 13.3^\circ$  between the moiré vector and the Earth’s gravitational vector. The uncertainties shown are purely from counting statistics.

shift induced by placing a well-characterized test mass alongside the interferometer. The enabling factor of the 2D PGMI is the ability to perform a single shot experiment with a broadband wavelength distribution and an *in situ* reference frame, thereby eliminating several sources of systematic errors.

**Conclusions.** We have expanded neutron phase-grating moiré interferometry to 2D and enabled the use of new degrees of freedom for material characterization studies and high-precision measurements of fundamental constants. We examined the manifestation and characterization of phase singularities in the moiré pattern by incorporating fork-dislocation phase gratings. Future studies will look at the interference between multiple phase singularities and the effects that would be introduced by samples with phase singularities such as skyrmions [40,41]. We also characterized two-PGMI setups that simultaneously manifest moiré interference along two orthogonal directions. The orthogonal interference pattern enables the presence of an *in situ* reference signal that can greatly reduce systematic errors. Furthermore, future studies will also examine the use of 2D phase-linear gratings with three-PGMI where it is possible to substantially increase the distance between the phase gratings. Whereas Eq. (4) is considering the neutron gravitation fall relative to the moiré period  $p_M$  at the camera, a three-PGMI has the capability to consider the neutron gravitation fall relative to the phase-grating period,  $\phi_g \propto 2\pi \Delta_y/p_G$ . Given that  $p_M \approx 10^3 p_G$ , this can provide an amplification to phase sensitivity by several orders of magnitude.

Furthermore, we can note that a typical sample that is used in neutron grating interferometers is a dilute solution of hard spheres with radius  $\approx 1\mu\text{m}$ . The effect of such a sample on the contrast is a well-behaved and known result

[35,42]. Therefore, the 2D PGMI is well positioned for studying gravitational forces on the micron scale by performing high-precision measurements that look for deviations from the mentioned expected contrast behavior. Future work will consider the details of this proposal.

**Acknowledgments.** This work was supported by the Canadian Excellence Research Chairs (CERC) program, the Natural Sciences and Engineering Research Council of Canada (NSERC) Discovery Program, Collaborative Research and Training Experience (CREATE) Program, the Canada First Research Excellence Fund (CFREF), and the National Institute of Standards and Technology (NIST) and the US Department of Energy, Office of Nuclear Physics, under Interagency Agreement No. 89243019SSC000025. The pulsed neutron experiment at J-PARC MLF was performed under a user program (Proposal No. 2022A0104).

**Appendix on the experimental methods and supporting data.** All phase gratings were fabricated out of silicon and had a target period of  $3\mu\text{m}$  and height of  $8.53\mu\text{m}$ . The height of  $8.53\mu\text{m}$  was chosen so that the grating imparts an optimal  $\pi/2$  phase shift for  $\lambda = 9\text{Å}$  neutrons. Figure 5 shows the SEM images of the four types of phase gratings that were fabricated.

The experiments with fork-dislocation phase gratings were performed at the ASTERIX facility at the Los Alamos Neutron Science Center (LANSCE) [43] with the wavelength distribution shown in Figure 6. The slit was  $500\mu\text{m}$  by  $500\mu\text{m}$  in size and the distance from the slit to the first phase grating (camera) was  $2.13\text{m}$  ( $4.25\text{m}$ ). The camera pixel size was  $50\mu\text{m}$  by  $50\mu\text{m}$ . The data acquisition time was  $\approx 20\text{min}$  at each grating separation distance. A detector normalization image was obtained by summing phase stepping measurements, where “phase stepping” refers to the translation of

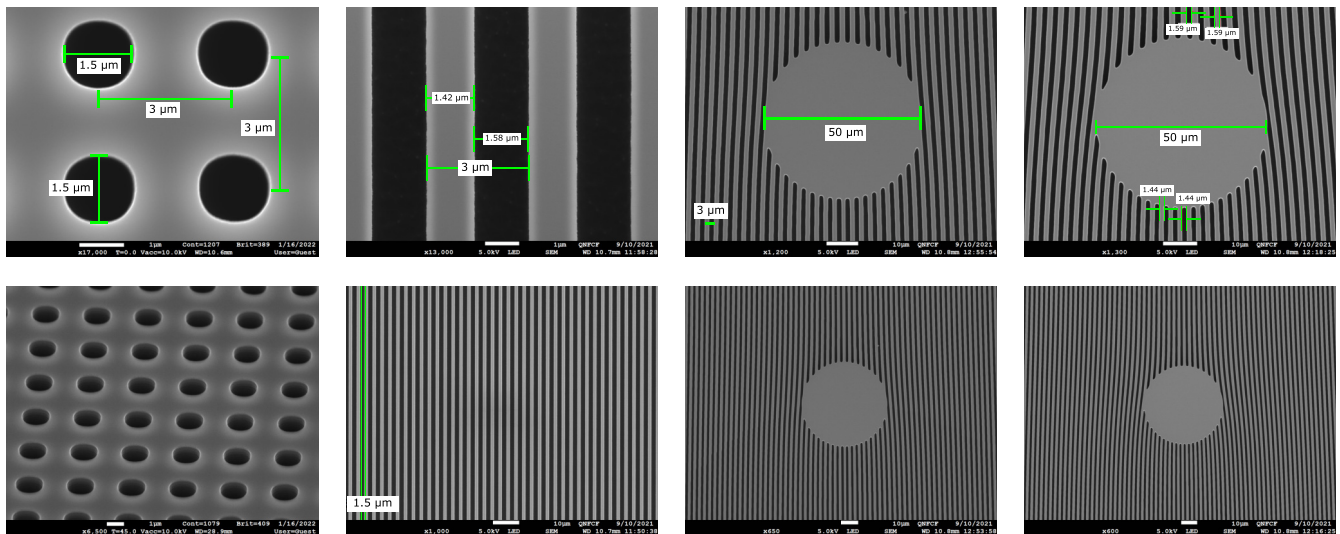


FIG. 5. SEM profiles of the phase gratings used in the experiments. All phase gratings were fabricated out of silicon and had a target period of  $3\mu\text{m}$  and height  $8.53\mu\text{m}$ . The first column depicts the 2D phase gratings, the second, third, fourth columns show the fork-dislocation phase grating with  $q = 0, 4, 7$ , respectively. The  $q = 0$  are the typical 1D phases gratings. There was a  $50\mu\text{m}$  mask covering the middle region of the  $q = 4$  and  $q = 7$  fork-dislocation phase gratings. This is a common practice to avoid the fabrication challenges associated with the higher aspect ratio near the phase singularity. In regards to the presented PGMI configurations, the masked region sets the resolution limit of the observable moiré phase singularity to  $\approx 100\mu\text{m}$ . Therefore the effect of this masked region is negligible.

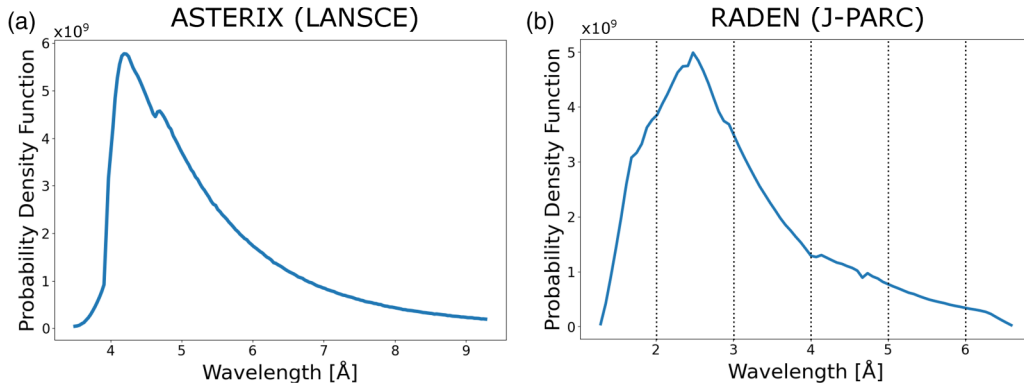


FIG. 6. (a) The wavelength distribution for the ASTERIX facility at the Los Alamos Neutron Science Center (LANSCE). This wavelength distribution was used for the data presented in Figs. 1(d) and 2. (b) The wavelength distribution for the RADEN facility at the Japan Proton Accelerator Research Complex (J-PARC). This wavelength distribution was used for the data presented in Figs. 3(c) and 4. The vertical lines show the four regions of the time-of-flight data used in Figs. 4(b) and 4(c).

one of the gratings along the grating vector direction [28]. Figure 7 shows the supporting data for the fork-dislocation phase-gratings experiments.

The experiments with the 2D phase gratings were performed at the the RADEN facility at the Japan Proton Accelerator Research Complex (J-PARC) [44] with the wavelength distribution shown in Figure 6. The 2D slit was composed of a sequence of two perpendicular 1D slits each made by bringing two cadmium pieces together with the target gap of 500  $\mu\text{m}$ . Two experimental setups were used, one for polychromatic measurements and the other with a neutron camera with lower dark counts ( $\approx 0$ ) for time-of-flight resolved measurements. For the first configuration the distance from the slit to the first phase grating (camera) was 4.16 m (8.30 m), the camera pixel size was 100  $\mu\text{m}$  by 100  $\mu\text{m}$ , and the image acquisition time was 4 h at each grating separation distance. For the second configuration the distance from the slit to the first phase grating (camera) was 4.23 m (8.53 m), the camera pixel size was 31  $\mu\text{m}$  by 31  $\mu\text{m}$ , and the data acquisition time was 5 h. For each setup configuration a detector normalization image was obtained from a measurement at a

grating separation of several centimeters that results in zero contrast. Figure 8 shows the supporting data for the 2D phase-grating experiments.

Double-side polished 10.16 cm diameter (100) silicon wafers were used to fabricate these gratings. A bilayer resist (PMGI/S1805 [45]) was patterned via a maskless aligner (MLA 150, Heidelberg Instrument). As a hard mask for the plasma etching, Cr metal (60 nm) was e-beam evaporated and lifted-off in heated PG Remover. A Bosch recipe was adopted to achieve a vertical sidewall etch profile. The samples were etched in an Oxford PlasmaLab ICP-380 inductively coupled plasma reactive ion etching (ICP-RIE) system, which provides high-density plasma with independently controlled system parameters. In our Bosch recipe, the passivation half cycle comprises the RF chuck power: 5 W, ICP coil power: 1000 W, C4F8: 160 sccm, pressure: 2.67 Pa, temperature: 15  $^{\circ}\text{C}$  for 5 s while the etch half cycle comprises the RF chuck power: 100 W, ICP coil power: 1000 W, SF6: 160 sccm, pressure: 3.33 Pa, temperature: 15  $^{\circ}\text{C}$  for 4 s. After fabricating the gratings, the remaining Cr mask was removed via plasma etching.

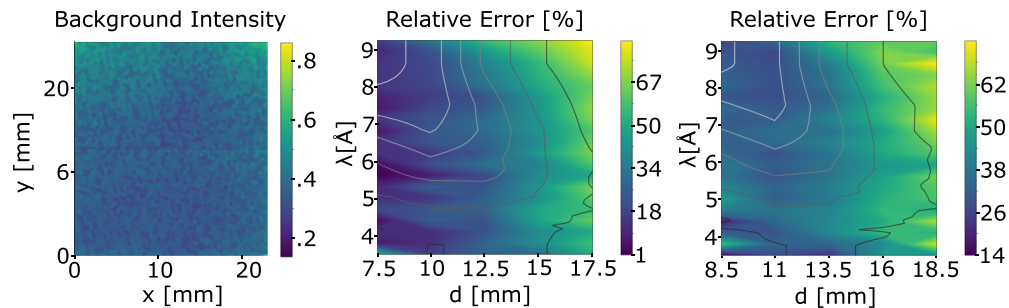


FIG. 7. Supporting data for fork-dislocation phase-gratings experiment presented in Figs. 1 and 2. (Left) Normalized background intensity profile that is used as the detector normalization image. (Middle) The residual plot for OAM = 4 data in Fig. 2 given given by  $100\% \times |simulation - data|/simulation$ . (Right) The residual plot for OAM = 7 data in Fig. 2 given by  $100\% \times |simulation - data|/simulation$ . Also shown are contour lines of constant contrast from Fig. 2. All of the simulations in this work were done with the k-space model described in Ref. [35].

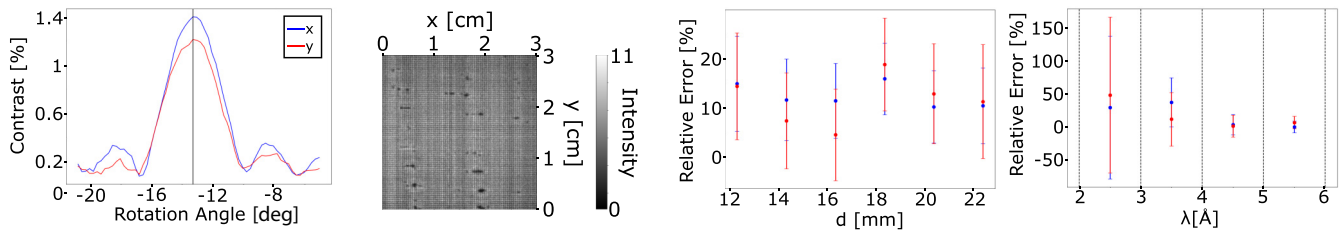


FIG. 8. Supporting data for the 2D phase-gratings experiment presented in Figs. 3 and 4. (Top left) Rotation vs contrast image for determining the the angle between the vertical moiré vector and the Earth's gravitational vector. Highest contrast occurs from  $\theta = 13.3^\circ$ . (Top right) Detector normalization image. Note that the square pattern is caused by camera effects and unrelated to the moiré pattern (bottom left) The residual plot for Fig. 4(b) given by  $100\% \times |simulation - data|/simulation$ . (Bottom right) The residual plot for Fig. 4(c) given by  $100\% \times |simulation - data|/simulation$ . All of the simulations in this work were done with the k-space model described in Ref. [35].

- [1] R. Colella, A. W. Overhauser, and S. A. Werner, Observation of gravitationally induced quantum interference, *Phys. Rev. Lett.* **34**, 1472 (1975).
- [2] H. Rauch, A. Zeilinger, G. Badurek, A. Wilfing, W. Bauspiess, and U. Bonse, Verification of coherent spinor rotation of fermions, *Phys. Lett. A* **54**, 425 (1975).
- [3] Y. Hasegawa, R. Loidl, G. Badurek, K. Durstberger-Rennhofer, S. Sponar, and H. Rauch, Engineering of triply entangled states in a single-neutron system, *Phys. Rev. A* **81**, 032121 (2010).
- [4] C. J. Wood, M. O. Abutaleb, M. G. Huber, M. Arif, D. G. Cory, and D. A. Pushin, Quantum correlations in a noisy neutron interferometer, *Phys. Rev. A* **90**, 032315 (2014).
- [5] C. W. Clark, R. Barankov, M. G. Huber, M. Arif, D. G. Cory, and D. A. Pushin, Controlling neutron orbital angular momentum, *Nature (London)* **525**, 504 (2015).
- [6] D. Sarenac, M. G. Huber, B. Heacock, M. Arif, C. W. Clark, D. G. Cory, C. B. Shahi, and D. A. Pushin, Holography with a neutron interferometer, *Opt. Express* **24**, 22528 (2016).
- [7] H. Lemmel, P. Brax, A. N. Ivanov, T. Jenke, G. Pignol, M. Pitschmann, T. Potocar, M. Wellenzohn, M. Zawisky, and H. Abele, Neutron interferometry constrains dark energy chameleon fields, *Phys. Lett. B* **743**, 310 (2015).
- [8] K. Li, M. Arif, D. G. Cory, R. Haun, B. Heacock, M. G. Huber, J. Nsofini, D. A. Pushin, P. Saggi, D. Sarenac, C. B. Shahi, V. Skavysh, W. M. Snow, and A. R. Young (The INDEX Collaboration), Neutron limit on the strongly-coupled chameleon field, *Phys. Rev. D* **93**, 062001 (2016).
- [9] A. Klein and S. Werner, Neutron optics, *Rep. Prog. Phys.* **46**, 259 (1983).
- [10] H. Abele, The neutron. Its properties and basic interactions, *Prog. Part. Nucl. Phys.* **60**, 1 (2008).
- [11] B. T. M. Willis and C. J. Carlile, *Experimental Neutron Scattering* (Oxford University Press, Oxford, 2017).
- [12] R. M. Thaler, Polarizability of the neutron, *Phys. Rev.* **114**, 827 (1959).
- [13] W. T. Fuhrman, J. Leiner, P. Nikolić, L. DeBeer-Schmitt, G. E. Granroth, M. B. Stone, M. D. Lumsden, P. A. Alekseev, J. M. Mignot, S. M. Koohpayeh, P. Cottingham *et al.*, Interaction driven subgap spin exciton in the Kondo insulator  $\text{SbB}_6$ , *Phys. Rev. Lett.* **114**, 036401 (2015).
- [14] F. Qian, L. J. Bannenberg, H. Wilhelm, G. Chaboussant, L. M. DeBeer-Schmitt, M. P. Schmidt, A. Aqeel, T. T. M. Palstra, E. Brück, A. J. E. Lefering *et al.*, New magnetic phase of the chiral skyrmion material  $\text{Cu}_2\text{OSeO}_3$ , *Sci. Adv.* **4**, eaat7323 (2018).
- [15] C. D. Dewhurst, M. Mochizuki, K. Yanai *et al.*, Néel-type skyrmion lattice with confined orientation in the polar magnetic semiconductor  $\text{GaV}_4\text{S}_8$ , *Nat. Mater.* **14**, 1116 (2015).
- [16] M. E. Henderson, B. Heacock, M. Bleuel, D. G. Cory, C. Heikes, M. G. Huber, J. Krzywon, O. Nahman-Levesqué, G. M. Luke, M. Pula *et al.*, Three-dimensional neutron far-field tomography of a bulk skyrmion lattice, *Nat. Phys.* **19**, 1617 (2023).
- [17] J. F. Clauser and S. Li, Talbot-von Lau atom interferometry with cold slow potassium, *Phys. Rev. A* **49**, R2213(R) (1994).
- [18] F. Pfeiffer, C. Grünzweig, O. Bunk, G. Frei, E. Lehmann, and C. David, Neutron phase imaging and tomography, *Phys. Rev. Lett.* **96**, 215505 (2006).
- [19] A. D. Cronin and B. McMorrin, Electron interferometry with nanogratings, *Phys. Rev. A* **74**, 061602(R) (2006).
- [20] C. David, B. Nöhammer, H. H. Solak, and E. Ziegler, Differential x-ray phase contrast imaging using a shearing interferometer, *Appl. Phys. Lett.* **81**, 3287 (2002).
- [21] A. D. Cronin, J. Schmiedmayer, and D. E. Pritchard, Optics and interferometry with atoms and molecules, *Rev. Mod. Phys.* **81**, 1051 (2009).
- [22] M. S. Chapman, C. R. Ekstrom, T. D. Hammond, J. Schmiedmayer, B. E. Tannian, S. Wehinger, and D. E. Pritchard, Near-field imaging of atom diffraction gratings: The atomic Talbot effect, *Phys. Rev. A* **51**, R14(R) (1995).
- [23] M. Busi, J. Shen, M. Bacak, M. C. Zdora, J. Čapek, J. Valsecchi, and M. Strobl, Multi-directional neutron dark-field imaging with single absorption grating, *Sci. Rep.* **13**, 15274 (2023).
- [24] H. Rauch and S. A. Werner, *Neutron Interferometry: Lessons in Experimental Quantum Mechanics* (Oxford University Press, New York, 2015).
- [25] P. Saggi, T. Mineeva, M. Arif, D. G. Cory, R. Haun, B. Heacock, M. G. Huber, K. Li, J. Nsofini, D. Sarenac *et al.*, Decoupling of a neutron interferometer from temperature gradients, *Rev. Sci. Instrum.* **87**, 123507 (2016).

- [26] H. F. Talbot, LXXVI. Facts relating to optical science. *No. IV*, *Philos. Mag.* **9**, 401 (1836).
- [27] H. Miao, A. Panna, A. A. Gomella, E. E. Bennett, S. Znati, L. Chen, and H. Wen, A universal moiré effect and application in x-ray phase-contrast imaging, *Nat. Phys.* **12**, 830 (2016).
- [28] D. A. Pushin, D. Sarenac, D. S. Hussey, H. Miao, M. Arif, D. G. Cory, M. G. Huber, D. L. Jacobson, J. M. LaManna, J. D. Parker, T. Shinohara, W. Ueno, and H. Wen, Far-field interference of a neutron white beam and the applications to noninvasive phase-contrast imaging, *Phys. Rev. A* **95**, 043637 (2017).
- [29] D. S. Hussey, H. Miao, G. Yuan, D. Pushin, D. Sarenac, M. G. Huber, D. L. Jacobson, J. M. LaManna, and H. Wen, Demonstration of a white beam far-field neutron interferometer for spatially resolved small angle neutron scattering, [arXiv:1606.03054](https://arxiv.org/abs/1606.03054).
- [30] D. Sarenac, D. A. Pushin, M. G. Huber, D. S. Hussey, H. Miao, M. Arif, D. G. Cory, A. D. Cronin, B. Heacock, D. L. Jacobson, J. M. LaManna, and H. Wen, Three phase-grating moiré neutron interferometer for large interferometer area applications, *Phys. Rev. Lett.* **120**, 113201 (2018).
- [31] A. J. Brooks, D. S. Hussey, H. Yao, A. Haghshenas, J. Yuan, J. M. LaManna, D. L. Jacobson, C. G. Lowery, N. Kardjilov, S. Guo *et al.*, Neutron interferometry detection of early crack formation caused by bending fatigue in additively manufactured SS316 dogbones, *Mater. Design* **140**, 420 (2018).
- [32] A. J. Brooks, G. L. Knapp, J. Yuan, C. G. Lowery, M. Pan, B. E. Cadigan, S. Guo, D. S. Hussey, and L. G. Butler, Neutron imaging of laser melted SS316 test objects with spatially resolved small angle neutron scattering, *J. Imag.* **3**, 58 (2017).
- [33] J. F. Nye and M. V. Berry, Dislocations in wave trains, *Proc. R. Soc. London, Ser. A* **336**, 165 (1974).
- [34] D. Sarenac, M. E. Henderson, H. Ekinici, C. W. Clark, D. G. Cory, L. DeBeer-Schmitt, M. G. Huber, C. Kapahi, and D. A. Pushin, Experimental realization of neutron helical waves, *Sci. Adv.* **8**, eadd2002 (2022).
- [35] D. Sarenac, G. Gorbet, C. Kapahi, Charles W. Clark, D. G. Cory, H. Ekinici, D. V. Garrad *et al.*, Cone beam neutron interferometry: From modeling to applications, *Phys. Rev. Res.* **6**, 023260 (2024).
- [36] E. Tiesinga, P. J. Mohr, D. B. Newell, and B. N. Taylor, CODATA recommended values of the fundamental physical constants: 2018, *J. Phys. Chem. Ref. Data* **50**, 033105 (2021).
- [37] C. Rothleitner and S. Schlamminger, Invited review article: Measurements of the Newtonian constant of gravitation, *Rev. Sci. Instrum.* **88**, 111101 (2017).
- [38] K. Kuroda, Anelasticity in G experiments, *Meas. Sci. Technol.* **10**, 435 (1999).
- [39] W. Michaelis, J. Melcher, and H. Haars, Supplementary investigations to PTB's evaluation of G, *Metrologia* **41**, L29 (2004).
- [40] P. Milde, D. Köhler, J. Seidel, L. M. Eng, A. Bauer, A. Chacon, J. Kindervater, S. Mühlbauer, C. Pfeleiderer, S. Buhrandt *et al.*, Unwinding of a skyrmion lattice by magnetic monopoles, *Science* **340**, 1076 (2013).
- [41] X. Yu, J. Masell, F. S. Yasin, K. Karube, N. Kanazawa, K. Nakajima, T. Nagai, K. Kimoto, W. Koshibae, Y. Taguchi, N. Nagaosa, and Y. Tokura, Real-space observation of topological defects in extended skyrmion-strings, *Nano Lett.* **20**, 7313 (2020).
- [42] M. Strobl, General solution for quantitative dark-field contrast imaging with grating interferometers, *Sci. Rep.* **4**, 7243 (2014).
- [43] R. O. Nelson, S. C. Vogel, J. F. Hunter, E. B. Watkins, A. S. Losko, A. S. Tremsin, N. P. Borges, T. E. Cutler, L. T. Dickman, M. A. Espy *et al.*, Neutron imaging at LANSCE—From cold to ultrafast, *J. Imag.* **4**, 45 (2018).
- [44] T. Shinohara, T. Kai, K. Oikawa, T. Nakatani, M. Segawa, K. Hiroi, Y. Su, M. Ooi, M. Harada, H. Iikura *et al.*, The energy-resolved neutron imaging system, RADEN, *Rev. Sci. Instrum.* **91**, 043302 (2020).
- [45] Certain trade names and company products are mentioned in the text or identified in an illustration in order to adequately specify the experimental procedure and equipment used. In no case does such identification imply recommendation or endorsement by the National Institute of Standards and Technology, nor does it imply that the products are necessarily the best available for the purpose.